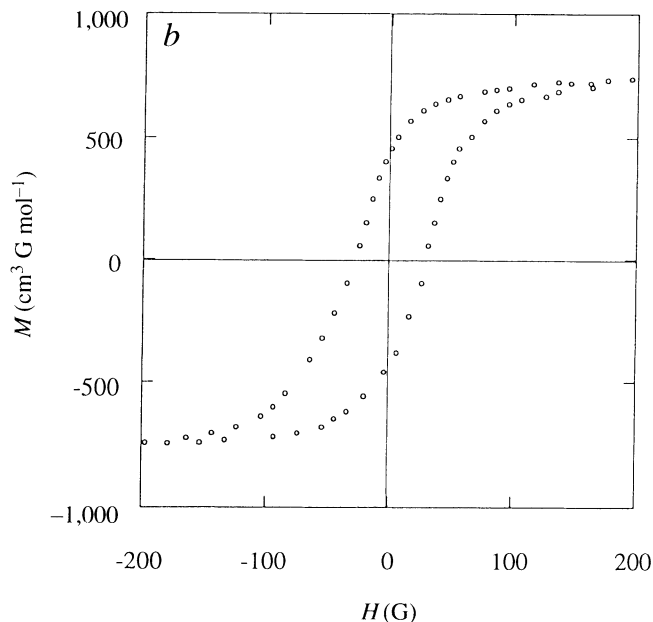FIG. 3 a, Plot of magnetization against applied field up to $H = 1$ kG of compound **1** at $T = 10$ K. Magnetization increases rapidly up to 200 G and then tends slowly to its saturation value $M_s \approx 0.15$ Bohr magneton, assuming a mean Lande g factor value $= 2$. The experimental saturation magnetization compares well with the computed value, using the V^{II} and V^{III} formula weight and antiferromagnetic coupling between chromium and vanadium: $M_s = |Ng\mu_B S_{total}|$ (N, Avogadro constant; μ_B, Bohr magneton); $S_{total} = [0.86 \times S_{Cr^{III}}] - [0.42 \times S_{V^{II}} + 0.58 \times S_{V^{III}}]$. With $S_{Cr^{III}} = 3/2$, $S_{V^{II}} = 3/2$, $S_{V^{III}} = 1$ and $g = 2$, $M_s = 0.16$ Bohr magneton. b, Hysteresis loop in the ± 200 G range at $T = 10$ K. The remanent magnetization is $M_r = 457$ cm^3 G mol^{-1} and the coercive field is $H_c = 25$ G.

therefore no ferromagnetic interaction between electrons in orthogonal orbitals (as in the dioxygen molecule, or as in $Cs^I Ni^{II}[Cr^{III}(CN)_6]$) (ref. 21). The number of magnetic neighbours and the strong antiferromagnetic interaction between noncompensated spins explain the high T_c. The three-dimensional ferrimagnetic approach illustrated by our result seems to be one of the most promising routes for designing further high-T_c magnets.

Although the interest of this finding is currently scientific rather than practical, one of the challenges with molecule-based magnets is to find applications as a result of their specific properties such as low density, transparency, insulating character, magneto-optical properties and tunable Curie temperatures[1–4]. We have already used the room-temperature Curie point, the sharp increase of the magnetization at T_c and absence of observable fatigue or deterioration during thermal cycles around the transition to design a temperature-sensitive magnetic switch. □

1. Miller, J. S. Angew. Chem. int. Edn Eng. **33**, 385–415 (1994).
2. Gatteschi, D. Adv. Mater. **6**, 635–645 (1994).
3. Verdaguer, M. et al. in Contributions to Development of Coordination Chemistry (eds Ondrejovic, G. & Sirota, A.) 19–24 (Slovak Tech. Univ. Press, Bratislava, 1993).
4. Kahn, O. Molecular Magnetism (VCH, New York, 1993).
5. Pei, Y., Verdaguer, M., Kahn, O., Sletten, J. & Renard, J. P. J. Am. chem. Soc. **108**, 7428–7429 (1986).
6. Kahn, O., Pei, Y., Verdaguer, M., Renard, J. P. & Sletten, J. J. Am. chem. Soc. **110**, 782–789 (1988).
7. Tamaki, H. et al. J. Am. chem. Soc. **114**, 6974–6979 (1992).
8. Day, P. Accts chem. Res. **12**, 236–243 (1979).
9. Descurtins, S. et al. Inorg. chim. Acta **216**, 65–73 (1994).
10. Stumpf, H. O., Ouahab, L., Pei, Y., Grandjean, D. & Kahn, O. Science **261**, 447–449 (1993).
11. Broderick, W. E., Thompson, J. A., Day, E. P. & Hoffman, B. M. Science **249**, 401–403 (1990).
12. Caneschi, A., Gatteschi, D., Renard, J. P., Rey, P. & Sessoli, R. J. Am. chem. Soc. **111**, 785–786 (1989).
13. Caneschi, A., Gatteschi, D., Sessoli, R. & Rey, P. Accts chem. Res. **22**, 392–398 (1989).
14. Miller, J. S., Calabrese, J. C., McLean, R. S. & Epstein, A. J. Adv. Mater. **4**, 298–300 (1992).
15. Nakazawa, Y. et al. Phys. Rev. B**46**, 8906–8914 (1992).
16. Allemand, P. M. et al. Science **253**, 301–303 (1991).
17. Chiarelli, R., Nowak, M. A., Rassat, A. & Tholence, J. L. Nature **363**, 147–149 (1993).
18. Manriquez, J. M., Yee, G. T., McLean, R. S., Epstein, A. J. & Miller, J. S. Science **252**, 1415–1417 (1991).
19. Lüdi, A. & Güdel, H. U., Stucki, H. & Lüdi, A. Inorg. chim. Acta **7**, 121–124 (1973).
20. Lüdi, A. & Güdel, H. U. in Structure and Bonding Vol. 14 (eds Dunitz, J. D. et al.) 1–21 (Springer, Berlin, 1973).
21. Gadet, V., Mallah, T., Castro, I., Veillet, P. & Verdaguer, M. J. Am. chem. Soc. **114**, 9213–9214 (1992).
22. Mallah, T., Thiébaut, S., Verdaguer, M. & Veillet, P. Science **262**, 1554–1557 (1993).
23. Entley, W. R. & Girolami, G. S. Inorg. Chem. **33**, 5165–5166 (1994).
24. Entley, W. R. & Girolami, G. S. Science **268**, 397–402 (1995).
25. Bozorth, R. M., Williams, H. J. & Walsh, D. E. Phys. Rev. **103**, 572–578 (1956).
26. Babel, D. Comments inorg. Chem. **5**, 285–320 (1982).
27. Anonymous, Miscellanea berolinensia ad Incrementum scientiarum Vol. 1, 377–378 (Berlin, 1710).
28. Nakamoto, K. Infra-red and Raman Spectra of Inorganic and Coordination Compounds 259–267 (Wiley, New York, 1978).
29. Wong, J., Lytle, F., Messmer, R. P. & Maylotte, D. H. Phys. Rev. B**30**, 5596–5610 (1984).
30. Néel, L. Annls Phys. **3**, 137–198 (1948).
31. Köningsberger, D. C. & Prins, R. (eds) X-ray Absorption (Wiley, New York, 1988).

Selective binding and removal of guests in a microporous metal–organic framework

O. M. Yaghi, Guangming Li & Hailian Li

Department of Chemistry and Biochemistry,
Goldwater Center for Science and Engineering,
Arizona State University, Tempe, Arizona 85287-1604 USA

MICROPOROUS inorganic materials such as zeolites find widespread application in heterogeneous catalysis, adsorption and ion-exchange processes. The rigidity and stability of such frameworks allow for shape- and size-selective inclusion of organic molecules and ions[1–4]. Analogous microporous structures based on organic building blocks have the potential for more precise rational design, through control of the shape, size and functionalization of the pores[5–8]. Here we report the synthesis of a metal–organic framework designed to bind aromatic guest molecules selectively. The basic building block is a symmetric organic molecule, which binds metal ions[9,10] to form layers of the metal–organic compound alternating with layers whose composition is determined by the functionalization of the starting molecules. The layers create channels in which guest aromatic molecules may be selectively bound. We show that the crystal lattice thus formed is thermally stable up to 350 °C, even after removal of included guest molecules, and that the inclusions can be selectively readsorbed.
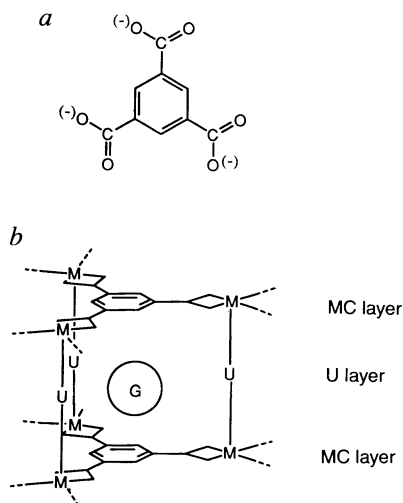
a

b

FIG. 1 *a*, Structural formula 1,3,5-benzenetricarboxylate (BTC), and *b*, its coordination to a metal ion to form alternating metal-carboxylate and spacer unit layers to form voids where guest inclusions are accommodated.

Our construction strategy uses symmetry and functionality of the starting molecular building block in its reaction with metal ions to support the formation of a covalent solid having the desired open framework[9,10]. Multidentate molecular components are used to enhance its thermal stability. We chose 1,3,5-benzenetricarboxylate (BTC) (Fig. 1*a*) as the building block as it has three equally spaced carboxylate groups linked to an aromatic ring to give it a rigid disk-like conformation. As carboxylate groups bind to transition metal ions within the same plane as either bidentate or monodentate ligands[11], the reaction of BTC with a first-row transition metal should yield a material composed of metal-carboxylate (MC) layers (Fig. 1*b*). We considered that these sheets might be made functional by using a method previously applied to layered vanadium phosphates[12] and lead halides[13], in which other molecular units (U) are introduced to occupy vacant metal sites lying perpendicular to the layers. The stacking of these layers in the crystal should produce alternating MC and U layers and, depending on the choice of U, a suitable environment for selective inclusion of guests (G) between the MC layers.

The success of this synthetic strategy was demonstrated by diffusing pyridine into mixture of the acid form of BTC and $Co(NO_3)_2$ in alcohol for three days to give a good yield of large, pink, cubic crystals which were insoluble in water and common organic solvents. The homogeneity of the bulk product was confirmed by comparison of the observed and calculated powder diffraction patterns obtained from single-crystal data. An X-ray crystal analysis on a single crystal from this reaction revealed the presence of a neutral porous network represented as $CoC_6H_3(COOH_{1/3})_3(NC_5H_5)_2 \cdot 2/3NC_5H_5$. A fragment of the structure is shown in Fig. 2, where three BTC units are coordinated to each of the Co(II) centres. One of the BTC units is completely deprotonated and coordinates to three metal centres in a bidentate fashion, whereas each of the other units coordinates to three metal centres as monodentate ligand; the remaining free carbonyls hydrogen-bond strongly to adjacent free carbonyls. The remaining positions on the metal centres are occupied by pyridine molecules, which we treated as being statistically disordered, with two preferred orientations around the Co–N bond. This arrangement generates extended sheets along the *x*–*y* plane. In the crystal these sheets stack along the *z*-axis to give alternating cobalt-carboxylate and pyridine layers (Fig. 3*a*). The cobalt-carboxylate layers are separated by 7 Å. The anchored pyridine ligands hold these layers tightly together by

mutual π-stacking, as is evident from the distance (4–6 Å) between pyridines. In the remaining space between the sheets there are uncoordinated pyridine molecules which occupy the rectangular channels (7 × 10 Å) that result from the tight fit between the layers. This gives the structure a three-dimensional character: in the direction perpendicular to the layers, the closely interacting pyridines form a rigid channel system. The separation between the layers and the channel structure remain unaltered when guests are removed or included (see below). It is therefore reasonable to consider this compound as being analogous to zeolites rather than to intercalation compounds. The pyridine guests π-stack with the benzene rings of BTC units of adjacent layers (Fig. 3*b*), where the distance between the pyridine π-system and that of BTC is 3.5 Å.

The π-stacking of both the coordinated pyridine ligands and the included pyridine guests have significant implications for the rigidity and selectivity of this porous framework. Thermal gravimetric analysis of a crystalline sample showed a weight loss of 11.7% at 190 °C, corresponding to the loss of the pyridine guests occupying the channels (2/3 NC_5H_5 per formula unit), followed at 350 °C by a further weight loss (45.5% of total), corresponding to the loss of the remaining pyridine molecules
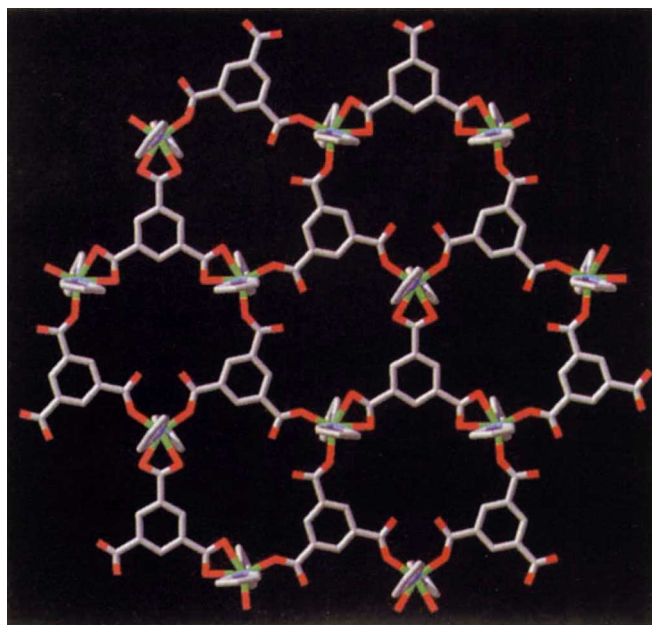

FIG. 2 A single layer of the extended porous network of $CoC_6H_3(COOH_{1/3})_3(NC_5H_5)_2 \cdot 2/3\ NC_5H_5$. The metal-carboxylate layer is shown approximately along the *x*–*y* plane: green, Co; red, O; blue, N; grey, C. Only one of the two preferred orientations about the Co–N bond is shown for the statistically disordered coordinated pyridine molecules. The hydrogen atoms on the pyridines and BTC units are omitted for clarity.

METHODS. Single crystals of this material at 20 ± 1 °C are hexagonal, of space group $P6_3/mcm$-D^3_{6h} (no. 193), with $a = 16.711(4)$ Å, $c = 14.189(2)$ Å; $V = 3,423(1)$ Å^3 and $Z = 6$ for $x = 1$, $d_{calc} = 1.464$ g cm^{-3}, μ_a (MoKα) = 0.80 mm^{-1}). A total of 1,161 independent reflections having 2θ (MoKα) < 50.7° (the equivalent of 0.8 limiting Cu Kα spheres) were collected on a computer-controlled Nicolet autodiffractometer using full (0.90° wide) ω scans and graphite monochromatic MoKα radiation. The structure was solved using direct methods techniques with the Siemens SHELXTL-PC software package, as modified at Crystalytics Company. The resulting parameters have been refined to converge (R_1 (unweighted, based on F) = 0.068 for 552 independent reflections having 2θ (MoKα) < 50.7° and $I > 3\sigma(I)$). Further details are available from the authors. The density of crystals freshly isolated from the mother liquor was measured by flotation as 1.48 ± 0.01 g cm^{-3}. Elemental microanalysis on crystalline samples of this material gave C, 54.99; H, 3.82; N, 7.44; Co, 12.43%; calculated values for $CoC_6H_3(COOH_{1\ 3})_3(NC_5H_5)_2 \cdot 2/3\ NC_5H_5$ were C, 56.11; H, 3.66; N, 7.82; Co, 12.33%.
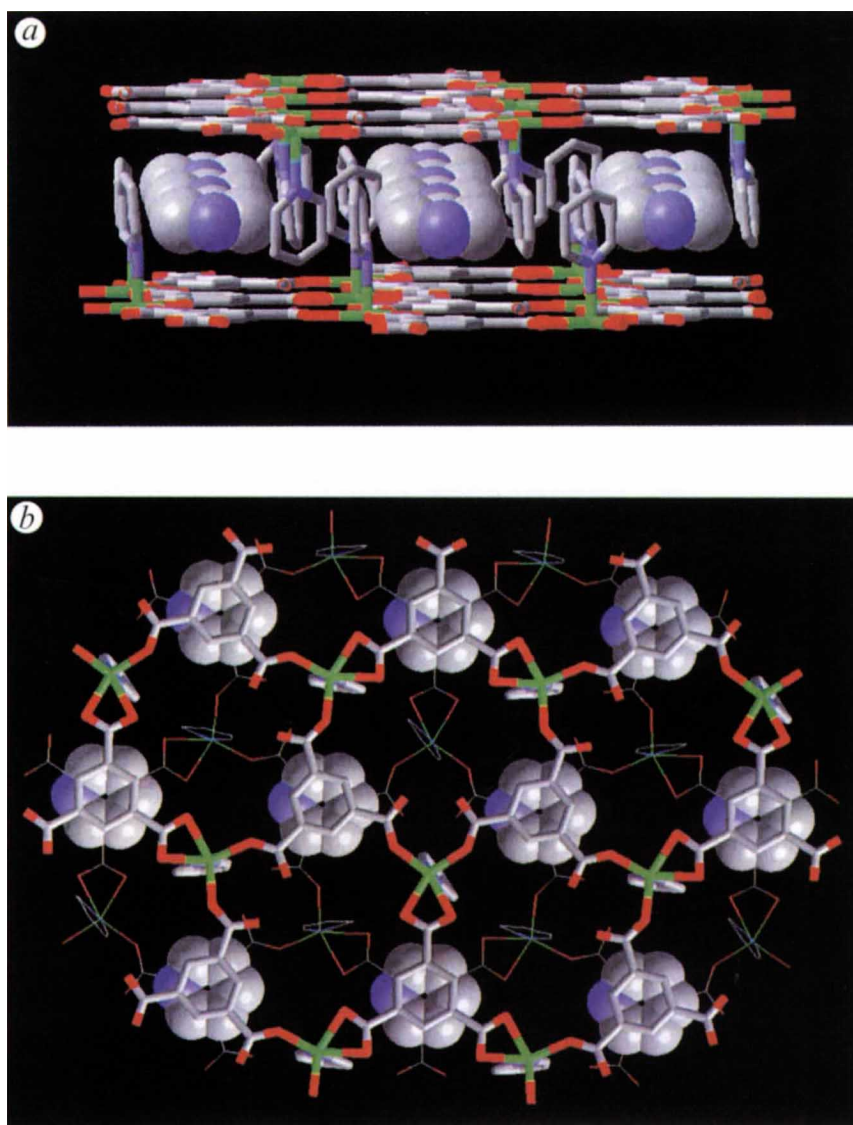
FIG. 3 a, A perspective drawing of the solid-state structure of $CoC_6H_3(COOH_{1/3})_3(NC_5H_5)_2 \cdot 2/3$ NC_5H_5 perpendicular to the z-axis. The cobalt-carboxylate layers with anchored pyridines are shown as line drawings for clarity. Pyridine guest molecules are represented by their space-filling van der Waals radii to show their occupation of the channels within the structure. b, View of the structure along the z-axis showing π-stacking of the pyridine guests with the benzene rings of BTC units. For clarity, the top layer is depicted in thicker lines than the lower layer. The colour scheme is the same as in Fig. 2. The pyridine guests in a and b were refined as six-membered carbon rings and centred about the $-3m$ site at the origin of the unit cell and the 32 site at (2/3, 1/3, 0) (further details available from the authors). Their representation as pyridine molecules and their orientation in the face-to-face mode with BTC is shown for clarity.

bound to the metal centres within the framework (2 NC_5H_5 per formula unit). This material remains crystalline upon removal of the pyridine inclusions. The X-ray powder pattern of a sample that has been heated to 200 °C for six hours shows that the positions and intensities of the most intense lines (002), (003), (004), (005) and (006) remain unchanged relative to those for an unheated sample of the solid. Elemental microanalysis for the heated material (measured values for C, 52.38; H, 3.46; N, 6.84%; calculated values for $CoC_6H_3(COOH_{1/3})_3(NC_5H_5)_2$ were C, 53.66; H, 3.32; N, 6.59) points to the absence of pyridine guests. Further heating of this sample to 350 °C reveals the absence of pyridine in the sample and a different X-ray diffraction pattern for the resulting solid. However, upon addition of pyridine the original pattern for the solid as synthesized is obtained. Presumably, the cobalt-carboxylate layer is preserved throughout the cycle of heating, cooling and inclusion. We are investigating this further to confirm the stability of the cobalt-carboxylate layer.

Examination of the single crystals with an optical microscope at 50 °C under a pressure of 0.001 mm Hg showed that they retain their morphology and crystallinity upon loss of the pyridine guests. We used infrared spectroscopy to show that solid samples of this material, from which the pyridine guests had been removed, selectively absorb aromatic molecules such as benzene, nitrobenzene, cyanobenzene and chlorobenzene, but not acetonitrile, nitromethane or dichloroethane. These experiments were done by suspending the solid in a solvent with aromatic and non-aromatic components; for example, 0.5 g solid was added to 1 ml of a 1:1 mixture of C_6H_5CN/CH_3CN as solvent and allowed to stand for less than 30 min. After filtration and drying, a solid containing C_6H_5CN but no CH_3CN was obtained. The Fourier transform of the infrared spectrum of the resulting solid showed a peak at v_{CN} at 2,231 cm^{-1}, corresponding to that of C_6H_5CN, and nothing in the range 2,240–2,260 cm^{-1}, where aliphatic non-conjugated nitriles like acetonitrile are expected to appear. Analogous experiments for 1:1 mixtures of the solvents $C_6H_5NO_2/CH_3NO_2$, C_6H_6/CH_3NO_2 and $C_6H_5Cl/C_2H_5Cl_2$ showed that the solid consistently had greater selectivity for inclusion of the aromatic solvent. In each case the diffraction pattern of the resulting sample was similar to that of the original material—the line positions remain unchanged, although the intensities changed slightly. This indicates that the crystal lattice is preserved and the distance between the cobalt-carboxylate layers is constant. We believe that the remarkable selectivity of this open framework towards aromatic molecules is a direct consequence of their π-stacking with the BTC units within the sheets. The use of multidentate ligands such as BTC coupled with the functionalization of the framework contributes greatly to the unusual thermal stability of this material. In conclusion, our results demonstrate the application of molecular chemistry in the design of thermally stable open and rigid frameworks capable of selective inclusion.   □

1. Komarneni, S., Smith, D. M. & Beck, J. S. (eds) *Advances in Porous Materials* (Materials Research Society, Pittsburgh, 1995).
2. Ribeiro, F. R., Rodrigues, A. E., Rollmann, L. D. & Naccache, C. (eds) *Zeolites: Science and Technology* (Nijhoff, The Hague, 1984).
3. Dyer, A. *An Introduction to Zeolite Molecular Sieves* (Wiley, Chichester, 1988).
4. Hölderich, W., Hesse, M. & Näumann, F. *Angew. Chem. int. Edn engl.* **27**, 226–246 (1988).
5. Yaghi, O. M. & Li, G. *Angew. Chem. int. Edn engl.* **34**, 207–209 (1995).
6. Gardner, G. B., Venkataraman, D., Moore, J. S. & Lee, S. *Nature* **374**, 792–795 (1995).
7. Abrahams, B. F., Hoskins, B. F., Michall, D. M. & Robson, R. *Nature* **369**, 727–729 (1994).
8. MacGillivray, L. R., Subramanian, S. & Zaworotko, M. J. *J. chem. Soc., chem. Commun.* 1325–1326 (1994).
9. Yaghi, O. M., Sun, Z., Richardson, D. A. & Groy, T. L. *J. Am. chem.Soc.* **116**, 807–808 (1994).
10. Hoskins, B. F. & Robson, R. *J. Am. chem. Soc.* **112**, 1546–1554 (1990).
11. Wilkinson, G., Gillard, R. D. & McCleverty, J. A. *Comprehensive Coordination Chemistry: The Synthesis, Reactions, Properties and Applications of Coordination Compounds 5; Late Transition Elements* (Pergamon, Oxford, 1987).
12. Johnson, J. W. et al. *J. Am. chem. Soc.* **111**, 381–383 (1989).
13. Calabrese, J. et al. *J. Am. chem. Soc.* **113**, 2328–2330 (1991).

Influence of mountain ranges on the mid-latitude atmospheric response to El Niño events

Eric DeWeaver & Sumant Nigam

Department of Meteorology, University of Maryland College Park, Maryland 20742-2425, USA

TROPICAL heating associated with El Niño events influences weather patterns around the globe[1-4], in part by generating wave-like disturbances of vorticity (a measure of local fluid circulation about the vertical) in the upper troposphere which extend into the mid-latitude regions. But these waves do not account well for the observed mid-latitude consequences of El Niño[5-8] events. Here we show that a secondary interaction of these waves with mid-latitude mountains contributes significantly to the observed flow patterns. On encountering a mountain, a column of rotating air is compressed vertically, spreads horizontally, and its net vorticity is thereby reduced. For a realistic distribution of El Niño-related tropical heating, we find that vortex compression, primarily in the Himalayan–Tibetan region, generates a vorticity contribution at mid-latitudes with an amplitude up to one-half that of the directly propagating wave-train. Mountains therefore play a significant role in determining the structure of the extratropical response to El Niño.

To examine the forcing of circulation anomalies, or departures from climatology, accompanying El Niño events, we attempted to simulate the difference in upper-level rotational flow between recent El Niño and La Niña winters using a spectral divergent steady-state barotropic model[6]. The large-scale flow in the upper troposphere consists mainly of horizontal motions which, outside regions of deep tropical heating, are largely non-divergent. Thus it is reasonable to diagnose global flow anomalies by modelling the vertical component of vorticity[6], referred to here simply as 'vorticity'. On these spatial scales, the dominant source of vorticity is the conversion of the Earth's vorticity (as manifested in the Coriolis force) to flow vorticity by divergent motions, an effect analogous to the induction of electric currents in a wire loop moving through a magnetic field. In comparison to this mechanism, generation of vorticity by processes such as vertical advection, pressure-density solenoids, and tilting, can be neglected to first order. The resulting equation is generally referred to as the barotropic vorticity equation[9].

In this study, we simulated the 200-hPa streamfunction (Ψ_{200}) differences between the 1987/88 (El Niño) and 1988/89 (La
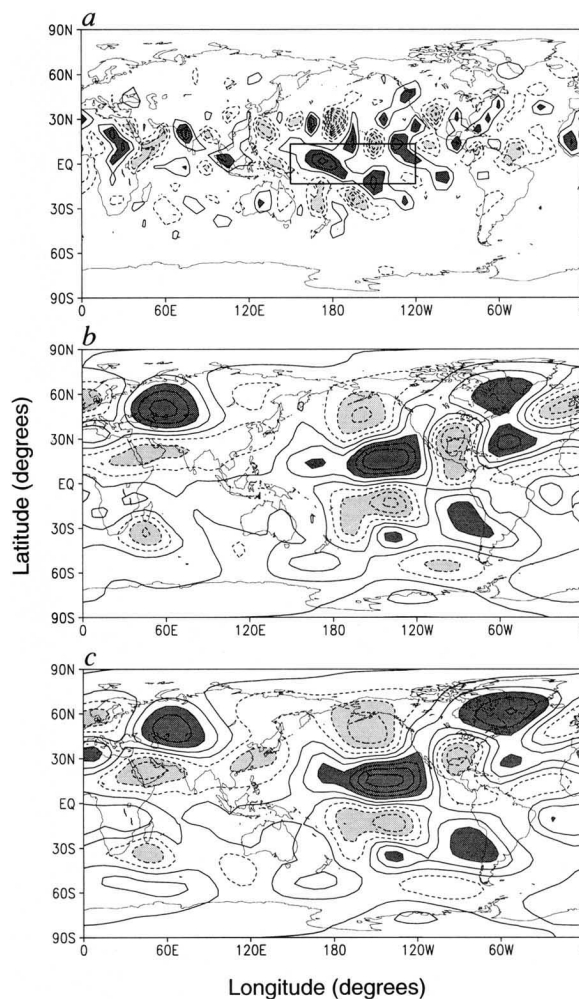

FIG. 1 Divergence and rotational flow anomalies at the 200 hPa level in the atmosphere between the winters (December, January, February) of 1987/88 and 1988/89. a, χ-derived divergence anomaly ($10^{-6}\,s^{-1}$) with zero contour suppressed, and with dark (light) shading for positive (negative) anomalies in excess of $2 \times 10^{-6}\,s^{-1}$; b, simulated Ψ_{200} anomaly with the zonal-mean component removed; c, corresponding Ψ_{200} anomaly from ECMWF analyses. Contour interval is $3 \times 10^6\,m^2\,s^{-1}$, and values greater (less) than $\pm 6 \times 10^6\,m^2\,s^{-1}$ are heavily (lightly) shaded in b and c. The rectangular box in panel a defines the El Niño-related divergence anomaly used in the regional forcing experiments shown in Figs 2 and 3.

METHODS. Results displayed here are obtained from a diagnostic barotropic spectral model truncated rhomboidally at wavenumber 15, with Rayleigh damping $r = 0.2\,d^{-1}$ and biharmonic viscosity $v = 10^{16}\,m^4\,s^{-1}$. Rotational flow anomalies are obtained by solving the following equation for ψ_a using matrix inversion:

$$\mathbf{V}_{\psi_a} \cdot \nabla(\zeta_c + f) + \mathbf{V}_c \cdot \nabla\zeta_a + \zeta_a\nabla \cdot \mathbf{V}_{\chi_c} + (r + v\nabla^4)\zeta_a$$
$$= -(\zeta_c + f)\nabla \cdot \mathbf{V}_{\chi_a} - \mathbf{V}_{\chi_a} \cdot \nabla(\zeta_c + f) - \nabla \cdot (\overline{\mathbf{V}'\zeta'})_a$$

Here the climatological quantity ( )$_c$ is the average of that quantity for periods 1 and 2, and the anomaly ( )$_a$ is the difference. f is the planetary vorticity, ζ is the relative vorticity, χ is the velocity potential, and V_χ and V_ψ are the divergent and rotational parts of the wind field. This model solves for both the zonal-mean and eddy (zonally asymmetric) anomalies. The term on the extreme right hand side of the above equation represents the forcing by transient vorticity-flux convergence, while the first two terms represent anomalous vorticity generation by vortex-tube stretching and divergent advection of climatological vorticity. In the transient term, the overbar represents the seasonal average of the product, and the primes denote departures of V and ζ from their seasonal averages. The χ-problem is first solved for each winter season under the given model parameters.